Materials Science and Engineering A 550 (2012) 214–221

Contents lists available at SciVerse ScienceDirect

Materials Science and Engineering A

journal homepage: www.elsevier.com/locate/msea

Sub-micrometre holotomographic characterisation of the effects of solution heat treatment on an AlMg7.3Si3.5 alloy

D. Tolnai[a,b,*], G. Requena[a], P. Cloetens[c], J. Lendvai[b], H.P. Degischer[a]

[a] Institute of Materials Science and Technology, Vienna University of Technology, Karlsplatz 13/308, A-1040 Vienna, Austria
[b] Eötvös Loránd University, Department of Materials Physics, POB 32, HU-1518 Budapest, Hungary
[c] European Synchrotron Radiation Facility, 6 Rue Jules Horowitz, F-38000 Grenoble Cédex, France

ARTICLE INFO

Article history:
Received 1 December 2011
Received in revised form 12 April 2012
Accepted 17 April 2012
Available online 23 April 2012

Keywords:
Synchrotron tomography
Aluminium alloys
Coarsening
Mechanical characterisation
Cast Al–Mg–Si alloys

ABSTRACT

A strip cast AlMg7.3Si3.5 alloy is investigated by sub-micrometre holotomographic analysis achieving a voxel size of $(60\,nm)^3$ by cone beam magnification of the focused synchrotron beam using Kirkpatrick–Baez mirrors. The three-dimensional microstructure of the same specimen volume in the as-cast state is compared with that after exposure to 540 °C for 30 min resolving microstructural features down to 180 nm. The three-dimensional analysis of the architecture of the eutectic Mg_2Si and the Fe-aluminides reveals how the as-cast microstructure changes during the solution treatment. The alloy in the as-cast condition contains a highly interconnected seaweed-like Mg_2Si eutectic. The level of three-dimensional interconnectivity of the Mg_2Si eutectic phase decreases by only partial disintegration during the heat treatment correcting the two-dimensional metallographic impression of isolated round particles. Statistical analyses of the particle distribution, sphericity, mean curvatures and Gaussian curvatures describe quantitatively the architectural changes of the Mg_2Si phase. This explains the decrease of the high temperature strength of the alloy by the solution treatment tested in hot compression.

1. Introduction

Cast AlMgSi alloys are potential candidates to be used in automotive and aerospace application [1,2]. This system consists of α-Al dendrites with up to 1 vol.% Mg_2Si precipitates, α-Al/Mg_2Si eutectic and iron aluminides originating from Fe and Mn impurities [3]. A surplus of Si with respect to the stoichiometric ratio of the Mg_2Si phase (1.74:1) results in the formation of a ternary eutectic α-Al/Mg_2Si/Si at the end of the solidification [4,5]. The microstructure of the system has been characterised by various experimental methods such as calorimetry [6], crystallography [7,8], 2D and 3D metallography [5,9]. Two-dimensional (2D) metallographic investigations revealed the 'Chinese-script' shape of the Mg_2Si phase and needle-like Fe-rich aluminides [10]. Three-dimensional (3D) investigations show that the eutectic Mg_2Si presents a highly interconnected coral-like structure, while the shape of the aluminides ranges from needles to platelets [5,11,12].

The mechanical properties of multiphase materials are strongly dependent on the internal architecture of the constituent phases [13]. Thus, the determination of morphological parameters, like size, shape and interconnectivity of the phases or contiguity between them [14] are important to understand their macroscopic behaviour. Giving an appropriate description of the microstructure of such heterogeneous cast alloys usually requires the use of 3D characterisation methods [15,16], whereas the extrapolation from 2D to 3D is only possible to some extent by applying certain structural assumptions deduced from 3D images [17].

Synchrotron based microtomography (SCT) is a unique non-destructive imaging tool applicable to materials due to the high brilliance of the source and the transversal coherence of the beam [18]. Various multiphase materials have been imaged by SCT [5,13,19,20–22]. The transversal coherence of the beam can be exploited to produce phase contrast to reveal phases with similar X-ray attenuations [23]. Furthermore, phase retrieval (holotomography) can be performed for accurate quantitative analysis [24]. Due to the parallel nature of a synchrotron beam the resolution achieved by imaging is limited by the detector system (max. resolution $\sim 1\,\mu m \geq 3$ voxel edges). This can be improved by using different X-ray optical elements to focus the beam emitted in the synchrotron and exploiting the magnification achievable by cone beam radiation [25–28].

The aim of this study is to describe the fine internal architecture of a strip cast AlMg7.3Si3.5 alloy by high resolution SCT and to quantify the morphological changes due to a short solution heat

* Corresponding author at: Magnesium Innovation Centre, Helmholtz-Zentrum Geesthacht, Max-Planck-Strasse 1, D21502 Geesthacht, Germany.
Tel.: +49 4152 87 1974; fax: +49 4152 87 1974.
E-mail address: domonkos.tolnai@hzg.de (D. Tolnai).

0921-5093/$ – see front matter © 2012 Elsevier B.V. All rights reserved.
http://dx.doi.org/10.1016/j.msea.2012.04.060

treatment. The results are used to explain the changes of the elevated temperature strength determined by compression tests of overaged samples suppressing precipitation hardening.

2. Experimental

2.1. Material

The studied material is a strip cast AlMg7.3Si3.5 alloy containing altogether ~0.5 wt% of Fe and Mn impurities, produced 2005 by the research group Alcan Aluminium Pechiney Aluval, Voreppe, France. The 50 cm wide strip was cast between steel rolls in a thickness of 5 mm. The Mg to Si wt% ratio of 2.1 in the AlMg7.3Si3.5 alloy is higher than the stoichiometry ratio of Mg_2Si (1.74:1), therefore no ternary eutectic α-Al/Mg_2Si/Si is expected. The same volume of the same sample was investigated by magnified synchrotron holotomography in as-cast condition and after solution treatment at 540 °C for 30 min. The samples were cooled down in air after the solution treatment.

2.2. Electron microscopy

Scanning electron microscopy (SEM) was performed with a FEI Quanta 200 FEG-SEM. The aluminium matrix was deep etched by a 1:10 NaOH/H_2O solution for 5 min to reveal the filigree architecture of the remaining eutectic Mg_2Si and Fe-aluminides.

2.3. Mechanical tests

HB 1/10 Brinell hardness tests were performed in the as-cast and solution treated (540 °C/30 min) conditions.

Compression tests were carried out at 300 °C with a Baehr T-805 dilatometer equipped with a deformation rig able to reach forces up to 25 kN. An initial strain rate of 1.25×10^{-3} s^{-1} was applied to the as-cast and the solution treated samples of 4 mm in diameter and 8 mm in length. 2 samples per condition were tested. Prior to the tests the samples were subjected to an overaging heat treatment at 300 °C for 2 h to minimise the strengthening effect of Mg_2Si precipitates and its changes during these elevated temperature tests.

2.4. Magnified synchrotron holotomography

Magnified cone beam synchrotron holotomography was carried out at the nano-imaging endstation ID22NI [27] of the European Synchrotron Radiation Facility (ESRF), Grenoble, France. A parallel synchrotron beam with an energy of 17.5 keV was focused using Kirkpatrick–Baez mirrors. 1200 projections of 1500 × 1500 pixels were acquired between 0 and 360° at four different sample-to-focal-point distances: 29.68, 30.6, 34.6 and 44.61 mm. The exposure time during acquisition was 1 s for each projection and the detector pixel size was 2.4 μm [29]. The focal-point-to-detector distance was kept fixed at 1185 mm. This resulted in a minimum effective pixel sizes of $(60\,nm)^2$. Efficient phase retrieval for the holotomographic reconstruction was achieved from the recordings at the four sample-to-focal-point distances [24]. Further experimental details are discussed in [28].

The sample imaged in the as-cast condition was subjected to a solution heat treatment at 540 °C for 30 min and magnified cone beam synchrotron holotomography was then repeated for the same region. The overaging heat treatment at 300 °C for 2 h has not been applied to the tomography samples. The overaged precipitates within the α-Al-dendrites are smaller than 180 nm, which cannot be resolved by the tomography experiments. Therefore the presence of coarser Mg_2Si precipitates does not influence the tomographic analysis of the larger eutectic Mg_2Si remains practically unchanged at 300 °C.

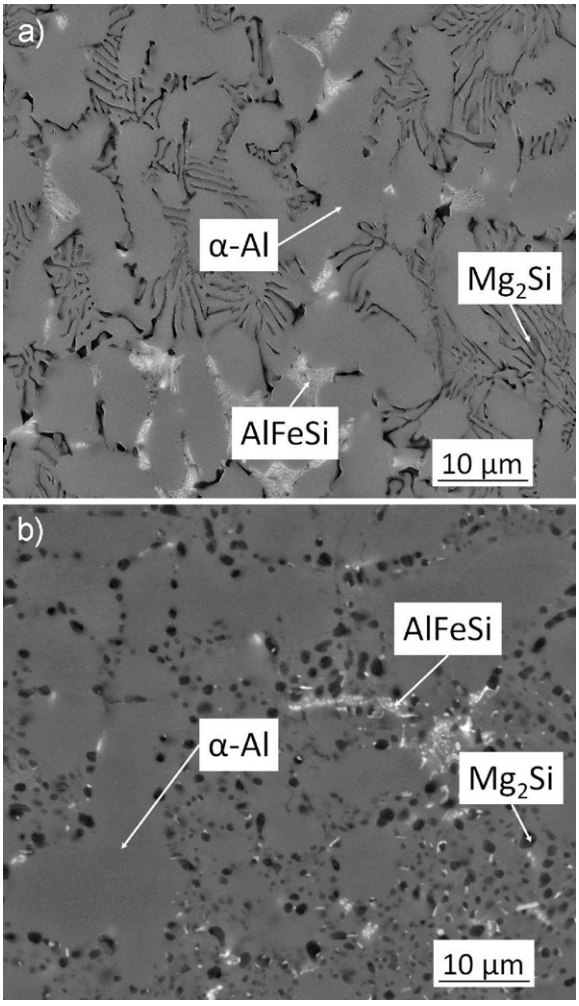

Fig. 1. Back scattered electron (BSE) micrographs of AlMg7.3Si3.5 in (a) as-cast and (b) solution treated (540 °C/30 min) conditions.

2.5. Segmentation and image pre-processing

Gaussian and anisotropic diffusion filtering were performed on the 32-bit images after the holotomographic reconstruction. The 3D segmentation of the phases was done based on the grey-level distribution after image conversion to 8 bits. A single global thresholding was followed by a region growing algorithm (a detailed description of the algorithm is given in [30]), which takes into account the variation of the grey levels in the local environment of the phase considered. A morphological smoothing was then applied: the voxels outside the segmented region having 4 or more touching neighbours were added to the segmented phase, while voxels belonging to the segmented region and having only 1 touching neighbour were removed. Only particles wider than 3 voxels (180 nm), i.e. larger than 27 voxels ($>5.8 \times 10^{-3}$ μm^3) were considered for evaluation.

3. Results

3.1. Electron microscopy

Fig. 1a and b shows SEM micrographs of the investigated alloy in the as-cast and solution treated conditions, respectively. Three

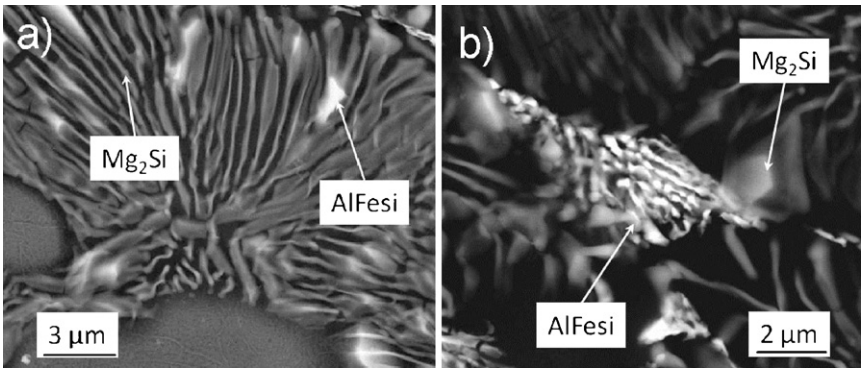

Fig. 2. High-resolution BSE images of the intermetallic phases after deep etching the α-Al: (a) Mg_2Si and (b) Fe-aluminides.

phases can be identified: (1) the α-Al dendrites (grey), (2) aluminide particles (AlFeSi) originating from the Fe and Mn impurities (white) and (3) the eutectic Mg_2Si phase (dark grey) embedded in eutectic Al [10]. The seaweed-like eutectic Mg_2Si (Fig. 1a) transforms into round and apparently isolated Mg_2Si particles during the solution treatment (Fig. 1b). The 3D interconnected structure formed by the eutectic Mg_2Si and the aluminides in the as-cast condition becomes visible after deep etching the Al (Fig. 2).

3.2. Mechanical tests

The HB 1/10 hardness decreases from 92.0 ± 0.5 in the as-cast condition to 68.2 ± 0.2 after the solution treatment (see Table 1). The results obtained during the elevated temperature compression tests are shown in Fig. 3. The curves show the mean of the two samples tested for each condition with the error bars indicating the scatter between them. The proof stress ($\sigma_{0.2}$) of the alloy also shows a decrease that goes from 60.0 ± 0.3 MPa in the as-cast condition to 39 ± 1 MPa after solution treatment. Softening is observed for the alloy in the as-cast condition after the maximum strength (σ_{max}) is reached at ~125 MPa. On the other hand, the alloy in the solution treated condition shows a steady state plastic deformation behaviour at a constant stress of ~90 MPa.

Table 1
Differences between the as-cast and solution treated conditions (3D quantitative analysis of the intermetallic phases refer to the same specimen region of 60 µm × 18 µm × 47 µm).

	As-cast	Solution treated (540 °C/30 min)
Hardness HB 1/10 (after overaging of 2 h/300)	92 ± 2	68.2 ± 0.2
Yield strength at 300 °C [MPa] (after overaging of 2 h/300)	60 ± 1	39 ± 1
Mg_2Si		
Number of particles	529	2884
Volume fraction V_f (vol.%)	19	16
V_f of the largest particle (vol.%)	17.9	11.8
Relative V_f of the largest particle (%)	91	73
Fe-aluminide		
Number of particles	235	855
Volume fraction V_f (vol.%)	1	1
Vol. of the largest particle (µm³)	56	54
Relative V_f of the largest particle (%)	10	10
Mean volume of the particles (µm³) (asymmetric half width of the distribution)	2.4 (12.9)	0.6 (6.5)

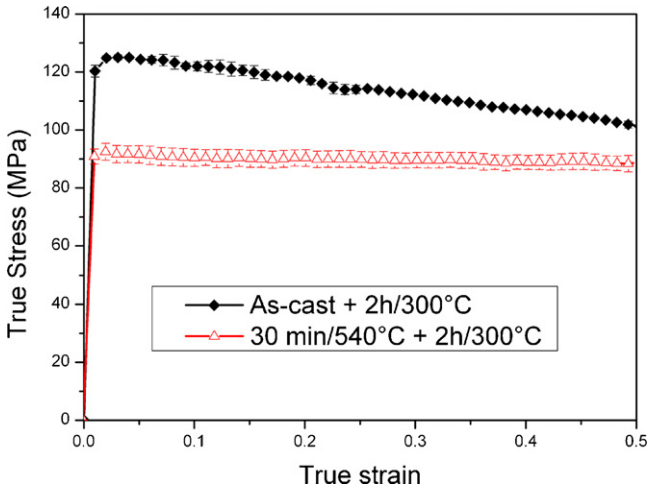

Fig. 3. Stress–strain curves obtained during compression tests at 300 °C.

3.3. Magnified synchrotron holotomography

Fig. 4a and b shows portions of reconstructed slices of the same region in the as-cast and the solution treated conditions, respectively. All phases, namely Mg_2Si, Fe-aluminides and α-Al, are resolved down to ~180 nm after the holotomographic reconstructions. Fig. 5a and b shows the eutectic Mg_2Si phase in the same

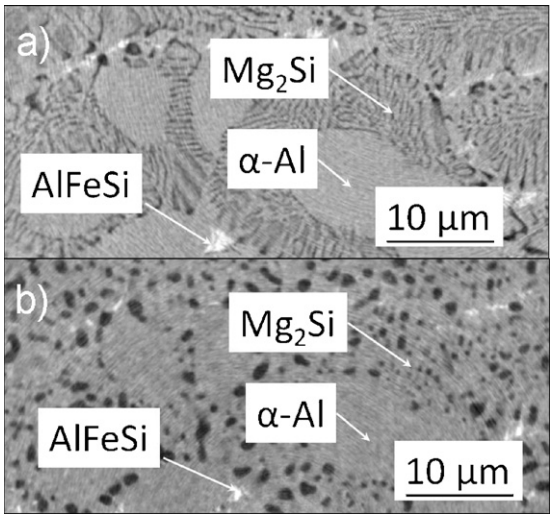

Fig. 4. Portions of reconstructed holotomographic slices of the AlMg7.3Si3.5 alloy: (a) as-cast condition and (b) solution treated condition. The pixel size is $(60\ nm)^2$.

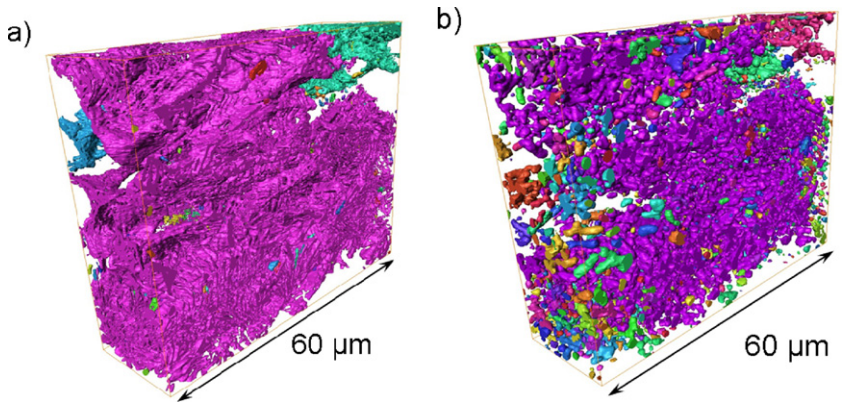

Fig. 5. Same rendered volumes (60 μm × 18 μm × 47 μm) of the Mg_2Si phase: (a) as-cast condition and (b) after 30 min/540 °C. The different colours indicate different Mg_2Si particles within the considered volume.

region (60 μm × 18 μm × 47 μm) in as-cast and solution treated conditions, respectively. The different colours represent different Mg_2Si particles within the investigated volume. The eutectic Mg_2Si phase presents a high interconnectivity and a seaweed-like structure in 3D that spheroidises and only partially fragments during the solution heat treatment. This is a remarkable difference with respect to the 2D images (Figs. 1b and 4b) in which the Mg_2Si network seems to transform into isolated particles.

3.4. Quantitative results

The results obtained by the 3D quantitative analysis for the number of particles, volume fraction (V_f) and interconnectivity of Mg_2Si and Fe-aluminides in the as-cast and the solution treated conditions in the same volume of 60 μm × 18 μm × 47 μm (Fig. 5) are summarised in Table 1. The interconnectivity is defined as the relative volume fraction of the largest individual particle (3D-connected feature) with respect to the total volume fraction of the investigated phase in the analysed volume.

This is a conservative analysis since particles located at the border of the volume (Fig. 5) might be connected if a larger volume were considered for analysis. The number of Mg_2Si particles increases by a factor >5 after the solution treatment, while the volume of the largest particle decreases by ~15%. The volume fraction of the largest Mg_2Si particle (interconnectivity) drops from 91% to 73%. These results quantify the partial disintegration of the highly interconnected 3D structure of Mg_2Si during solution treatment.

The number of Fe-aluminide particles increases by a factor >3, while the volume of the largest particle remains practically constant. The slightly reduced portion of the biggest particle is due to the newly resolved spheroidised particles shown in Fig. 6, which grow above the detection limit as a result of the coarsening that takes place during solution treatment. The contiguity (touching surface) between the eutectic Mg_2Si and Fe-aluminide was found to be negligible in the 3D analysis.

3.5. Sphericity

The sphericity, C_p, is calculated by (1), where V and S are the volume and the surface of a given particle, respectively [31]. Thus, $C_p = 1$ corresponds to a sphere, while $C_p = 0$ to an infinite plate. The C_p distribution of the Mg_2Si particles is shown in Fig. 7.

$$C_p = \frac{6\pi^{1/2}V}{S^{3/2}} \quad (1)$$

There is a slight shift towards higher sphericity values after solution treatment indicating that the particles become more convex-shaped.

The correlation between volume and sphericity of the Mg_2Si particles for the as-cast and the solution treated conditions are shown in Fig. 7b and c, respectively. Most of the large particles (width >0.5 μm) in the as cast state exhibit a complex structure (sphericity close to 0) which is transferred to Mg_2Si particles >5 μm after the heat treatment. The relative frequency maximum increases only from a sphericity of 0.8 to 0.85, but an additional population of bigger Mg_2Si particles is resolved in the heat treated condition.

3.6. Curvatures

The mean (K) and Gauss curvatures (H) [32,33], defined as the mean and the product of the principal curvatures, have been determined for the Mg_2Si particles in the as-cast condition and after the solution treatment using the software Avizo® [34]. A surface of the voxel-based volume of the segmented phase was rendered by a triangular approximation prior to the calculations. The osculate curves have been determined for each triangle of the rendered surface taking into account the neighbouring triangles up to the 2nd order. The local radii of these curves were averaged four times with the radii of direct neighbour triangles before the reciprocal value of the local radius was calculated. Surfaces which simultaneously exhibited mean and Gauss curvatures equal to zero were excluded from further evaluation in order to exclude the surfaces at the borders of the region of interest. The distributions are plotted in a mean versus Gaussian curvature coordinate system in Fig. 8.

A maximum is observed close to zero (flat surfaces) in the distribution of curvatures in the as-cast condition for the case where all the Mg_2Si particles are considered (Fig. 8a). Similarly, the maximum is close to zero for the biggest Mg_2Si particle and for the rest (Fig. 8b and c). The maximum for all the particles splits into two maxima after the solution treatment (Fig. 8a): one is still close to zero but displaced towards positive values of the mean curvature indicating a larger fraction of regions with a slight convex saddle shape; while the second peak moves into the positive–positive quadrant of the diagram (spheroid-like region). Furthermore, the Gauss curvature distribution is narrower after the solution treatment reducing its width mainly in the negative Gauss-curvature range (convex shapes). The extreme mean curvature values move from the negative–positive quadrant (pit shapes) towards higher values of the positive–positive quadrant (spheroid shapes). A very similar trend is observed for the largest Mg_2Si particle alone in the studied volume (Fig. 8b). The evolution of the curvatures of the

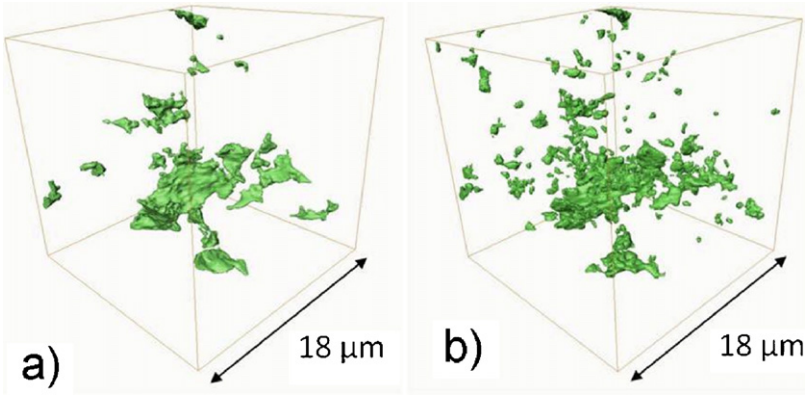

Fig. 6. Same rendered sub-volume $(18\,\mu m)^3$ of Fig. 5 showing the evolution of the Fe-aluminides in: (a) as-cast condition and (b) after 30 min/540 °C.

other particles changes similarly but more markedly by the solution treatment (Fig. 8c). The shift of the negative mean curvature values together with the corresponding positive Gauss curvature values towards zero is pronounced as well as the shift to higher positive–positive values (more spherical). These results show that the morphological changes are dominated by the morphology of the largest Mg_2Si particle that undergoes a slight process of local spheroidisation during the solution treatment.

3.7. Skeletonisation

The skeletonisation process performed with Avizo® [34] simplifies the 3D structure of the phases by applying a successive thinning algorithm and deleting voxels from the surface until the voxel distribution is transformed into linear sections that may be connected generating nodes [35]. Simplifying the shape of the eutectic Mg_2Si by applying skeletonisation also provides general information on the distribution of the lengths of the sections as shown in Fig. 9. The plotted lengths represent the distances between junctions and between the last junction and the end-points of the skeletonised branches. The skeletons of the same Mg_2Si particle are shown in Fig. 10 in as-cast condition and after 30 min/540 °C with its skeleton inside. The skeleton structure becomes less complex as the side branches disappear by spheroidisation during the solution treatment. The particle in Fig. 10a is represented by 6 line sections, which reduce to only one after the solution treatment. The shown particle is also getting shorter The number of the line sections in the largest Mg_2Si particle decreases by a factor of ~5 during solution treatment (from 41980 to 7978). The average section length in Fig. 9 increases with the solution treatment, while the probability of shorter lengths decreases resulting in an increase of ~50% of the mean section length (Fig. 9).

4. Discussion

The elevated temperature strength and the hardness of the material decrease after the solution heat treatment in a similar way as reported for eutectic Al–Si alloys [13]. The alloy in as-cast condition as well as after solution treatment was tested in an overaged condition (2 h/300 °C), to minimise precipitation strengthening. Therefore, its high temperature strength will be given mainly by the reinforcement's load carrying capability according to the properties and internal architecture of the rigid phases neglecting the unresolved precipitates. This architecture is formed by two independent rigid phases, namely the eutectic Mg_2Si and the Fe-aluminide particles, which are practically disconnected from each other. The Fe-aluminides resolved by the 3D analysis are $>(180\,\mu m)^3$. Such large particles cannot act as dispersoids to hinder dislocation gliding. Furthermore, their volume fraction amounts to only 1 vol.% (Table 1), which is below the minimum volume fraction necessary (~5 vol.%) to produce effective reinforcement in composites [36,37]. Therefore, the same contribution of the aluminides to the strength of the alloy in as cast and solution treated conditions is assumed as the morphological changes are negligible. Therefore, the aluminides' effect will not be discussed further.

The eutectic Mg_2Si presents a highly interconnected structure which can potentially reinforce the Al-matrix by a load transfer mechanism [38,39]. Its reinforcement capability will be given by its volume fraction, size, morphology, connectivity, spatial distribution and mechanical properties. Therefore, the decrease in strength

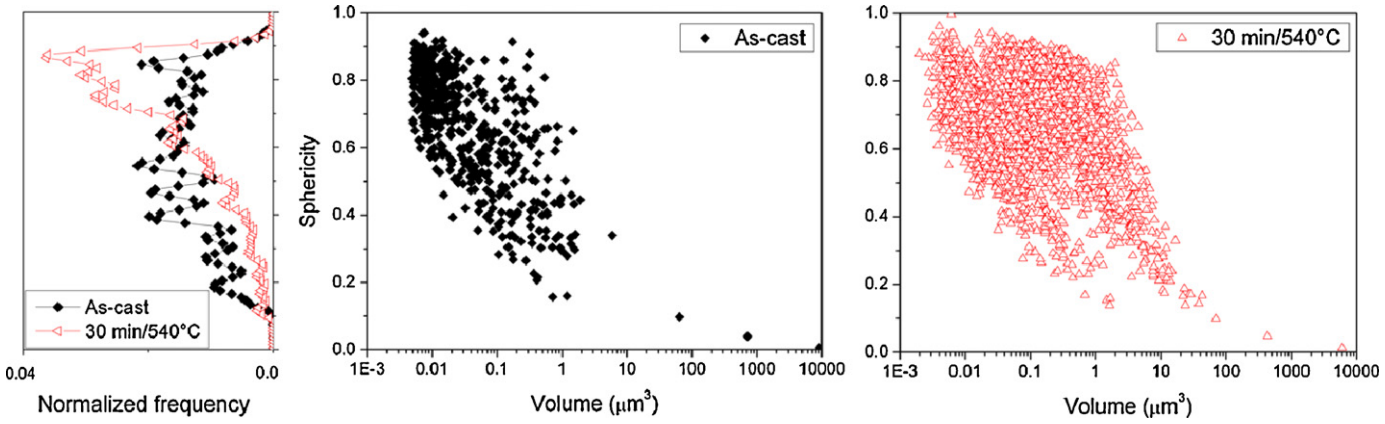

Fig. 7. Sphericity distributions of the Mg_2Si particles in as-cast condition and after 30 min/540 °C.

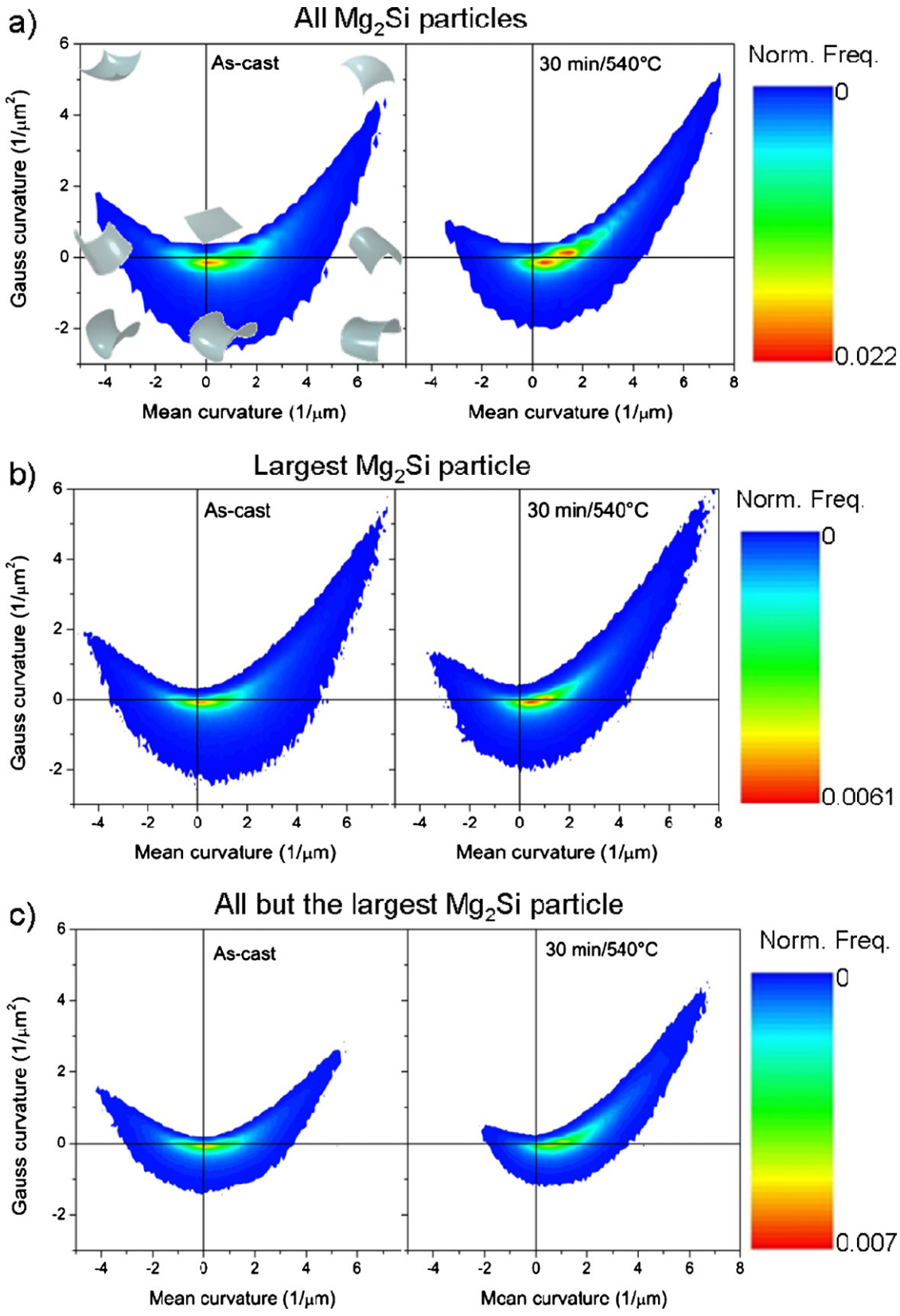

Fig. 8. Gauss versus mean curvature distributions of the surface of the Mg_2Si phase in a volume of (60 μm × 18 μm × 47 μm – see Fig. 5) (a) where all Mg_2Si particles in as-cast condition and after 30 min/540 °C are presented, (b) only the largest Mg_2Si particle in as-cast condition and after 30 min/540 °C, (c) all particles but the largest Mg_2Si particle in as-cast condition and after 30 min/540 °C.

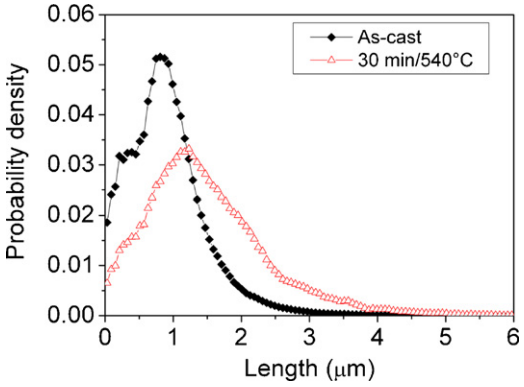

Fig. 9. Skeleton section length distribution of the Mg_2Si particles.

by the solution treatment observed in the compression tests at 300 °C (Fig. 3) is related to the changes in the Mg_2Si architecture. The volume fraction in the as-cast condition in the investigated volume amounts 19 vol.% and decreases to 16 vol.% after the solution heat treatment (see Table 1). The higher volume fraction in the as-cast condition is a result of segregation due to the fast cooling rate during the strip-cast process, which produces a Mg- and Si-enriched liquid. This solidifies eutectically with a higher amount of Mg_2Si than that of the equilibrium condition. Homogenisation takes place during solution heat treatment dissolving part of the Mg and Si from the eutectic Mg_2Si into the α-Al matrix producing a hardening potential by Mg_2Si precipitates, which results in the lower volume fraction of eutectic Mg_2Si resolved.

The spheroidisation process taking place during solution treatment (see Figs. 8 and 10) results in a partial fragmentation of the Mg_2Si particles. This may occur by pinch off fragmentation of the thin regions that results in disconnected particles. The partial fragmentation of the Mg_2Si structure is reflected by the increase by a factor of five of the number of Mg_2Si particles in the studied volume during the solution treatment. After this, further spheroidisation leads to the pronounced change observed in the shape of the fragmented particles, particularly the small ones in the range 6–10 μm^3 (see Fig. 8c) [40,35]. It is known that the introduction of hard particles in μm size-range to aluminium alloys does not increase the elevated temperature strength of the matrix (see e.g. [41]).

From the above discussion, it is possible to conclude that the changes in the internal architecture of the originally interconnected Mg_2Si structure that reduce the elevated temperature strength are: a decrease of ~20% in its interconnectivity (see Table 1), the spheroidisation of the Mg_2Si structure (see Figs. 5, 8 and 10) and a decrease of the volume fraction by about 3 vol.% of the eutectic Mg_2Si (see Table 1)

All these effects result in a decrease of $\sigma_{0.2}$ and σ_{max} by ~30% after the solution treatment with respect to the as-cast condition. Unfortunately, it is not possible to separate the individual contributions of each of those three effects based on the two conditions studied. The investigation of several solution treatment steps at the same temperature may help to separate the effect of each of those phenomena on the strength of this alloy.

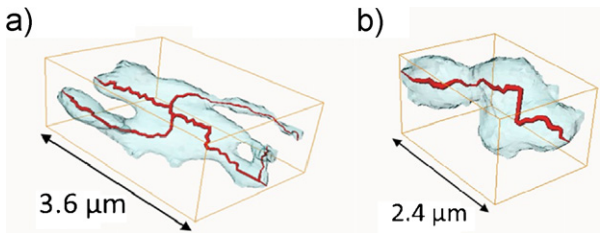

Fig. 10. The skeleton of the same Mg_2Si particle in (a) as-cast and in (b) solution treated condition.

5. Conclusions

The influence of microstructural changes on the elevated temperature strength of a strip cast AlMg7.3Si3.5 has been investigated in the as-cast condition and after 30 min/540 °C solution treatment by magnified synchrotron holotomography and by compression tests at elevated temperature. The following conclusions can be drawn from the results obtained for these two conditions suppressing precipitation hardening effects by overaging:

- Eutectic Mg_2Si ("Chinese script"), Fe-aluminides and α-Al were resolved in 3D down to a width of ~180 nm by magnified synchrotron holotomography. The eutectic Mg_2Si phase in the as-cast condition is almost completely interconnected (91%) forming a seaweed-like structure.
- The originally interconnected Mg_2Si structure partially fragments and spheroidises during the solution heat treatment reducing the interconnectivity to about 70%, whereas the 2D metallographic images suggest complete disintegration. The stereologic description of the Mg_2Si particles quantifies the spheroidisation by comparison of the curvatures, the sphericity and the skeletonised lengths distribution.
- The Fe-aluminides represent only 1 vol.% and there is practically no contiguity with the Mg_2Si phase. Some coarsening and spheroidisation occurs during the solution treatment.
- A decrease in Mg_2Si volume fraction from 19 to 16% takes place due to homogenisation of the fast cooled strip casting condition.
- The elevated temperature compressive strength ($\sigma_{0.2}$, σ_{max}) at 300 °C of the as-cast condition is about 30% higher than after the solution heat treatment. This is attributed to the loss of interconnectivity of Mg_2Si particles and to the reduced volume fraction of this phase.

Acknowledgements

The authors would like to thank the European Synchrotron Radiation Facility for the provision of synchrotron radiation facilities in the framework of proposal MA650. The University Service for Transmission Electron Microscopy (USTEM) of the Vienna University of Technology is acknowledged for the provision of the field emission gun scanning electron microscope. D. Tolnai, G. Requena and H.P. Degischer are grateful to the Austrian Science Fund (FWF30800080200 and FWF308000100201) and to the Austrian Agency for International Cooperation (WTZ HU 03/2010). D. Tolnai and J. Lendvai acknowledge the Hungarian Research Fund (OTKA-K-67692) and the Hungarian Research and Technology Foundation (TET AT-12/2009). H.P. Degischer acknowledges the assistance of M. Suery, SIMAP/INP-Grenoble and the guest scientist grant from CNRS-Rhone-Alpes 2005/06.

References

[1] F. Ostermann, Anwendungstechnologie Aluminium, Springer Verlag, Berlin/Heidelberg, 2007.
[2] Salzburger Aluminium AG, http://www.sag.at.
[3] L.F. Mondolfo, Al Alloys: Structures and Properties, Butterworth, London/Boston, 1976.
[4] http://www.thermocalc.com, Version 3.
[5] D. Tolnai, H.P. Degischer, J. Lendvai, Phys. Status Solidi A 206 (8) (2009) 1850–1854.
[6] H.B. Dong, R. Brooks, Mater. Sci. Eng. A 413–414 (2005) 480–484.
[7] M.V. Kral, H.R. McIntyre, M.J. Smillie, Scr. Mater. 51 (2004) 215–219.
[8] M.V. Kral, Mater. Lett. 59 (2005) 2271–2276.
[9] C. Li, Y.Y. Wu, H. Li, X.F. Liu, Acta Mater. 59 (2011) 1058–1067.
[10] H.P. Degischer, H. Knoblich, E. Maire, L. Salvo, M. Suery, Sbd. Prakt. Metallogr. Sonderband Praktischen Metallogr. 38 (2006) 67–74.

[11] F. Lasagni, A. Lasagni, M. Engstler, H.P. Degischer, F. Müklich, Adv. Eng. Mater. 10 (1–2) (2008) 62–66.
[12] E. Maire, J.C. Grenier, D. Daniel, A. Baldacci, H. Klöcker, A. Bigot, Scr. Mater. 55 (2) (2006) 123–126.
[13] G. Requena, G. Garcés, M. Rodriguez, T. Pirling, P. Cloetens, Adv. Eng. Mater. 11 (2009) 1007–1014.
[14] Z. Asghar, G. Requena, H.P. Degischer, P. Cloetens, Acta Mater. 57 (2009) 4125–4132.
[15] C.F. Mora, A.K.H. Kwan, Cem. Concr. Res. 30 (2000) 351–358.
[16] M.V. Kral, M.A. Mangan, G. Spanos, R.O. Rosenberg, Mater. Charact. 45 (2000) 17–23.
[17] A. Velichko, F. Mücklich, Prakt. Metallogr. 45 (2008) 423–439.
[18] European Synchrotron Radiation Facility, http://esrf.eu.
[19] D. Fuloria, P.D. Lee, D. Bernard, Mater. Sci. Eng. A 494 (2008) 3–9.
[20] G. Requena, H.P. Degischer, E. Marks, E. Boller, Mater. Sci. Eng. A 487 (2008) 99–107.
[21] A. Borbély, F.F. Csikor, S. Zabler, P. Cloetens, H. Biermann, Mater. Sci. Eng. A 367 (2004) 40–50.
[22] G. Requena, G. Fiedler, B. Seiser, P. Degischer, M. Di Michiel, T. Buslaps, Composites A 40 (2008) 152–163.
[23] J. Baruchel, J.-Y. Buffiére, E. Maire, P. Merle, G. Peix, X-Ray Tomography in Material Science, HERMES Science Publications, Paris, 2000.
[24] P. Cloetens, W. Ludwig, J. Baruchel, D. Van Dyck, J. Van Landuyt, J.P. Guigay, M. Schlenker, Appl. Phys. Lett. 75 (1999) 2912.
[25] P.J. Withers, Mater. Today 10 (12) (2007) 26–34.
[26] R. Mokso, P. Cloetens, E. Maire, W. Ludwig, J.Y. Buffiere, Appl. Phys. Lett. 90 (144104) (2007).
[27] A. Sakdinawat, D. Attwood, Nat. Photon. 4 (2010) 840–848.
[28] G. Requena, P. Cloetens, W. Altendorfer, C. Poletti, D. Tolnai, F. Warchomicka, H.P. Degischer, Scr. Mater. 61 (7) (2009) 760–763.
[29] J.-C. Labiche, O. Manthon, S. Pascarelli, M.A. Newton, G.G. Ferre, C. Curfs, G. Vaughan, A. Homs, D.F. Carreiras, Rev. Sci. Instrum. 78 (9) (2007) 1–11.
[30] http://metal.elte.hu/tomo3D.
[31] J. Ohser, F. Mücklich, Statistical Analysis of Micro Structures in Materials Science, John Wiley & Sons Ltd, Chichester, 2000.
[32] N.C.W. Kuijpers, J. Tirel, D.N. Hanlon, S. van der Zwaag, Mater. Charact. 48 (2002) 379–392.
[33] J. Osher, K. Schladitz, 3D Images of Materials Structures, Processing and Analysis, Wiley-VCH Verlag GmbH & Co. KGaA, Weinheim, 2009.
[34] http://vsg3d.com/node/25.
[35] Y. Zhou, A.W. Toga, IEEE Trans. Visual. Comp. Graph. 5 (3) (1999) 196–209.
[36] T.W. Clyne, P.J. Withers, An Introduction to Metal Matrix Composites, Cambridge University Press, Cambridge, 1993.
[37] C.M. Friend, J. Mater. Sci. 22 (1987) 3005–3010.
[38] F. Lasagni, J. Acuña, H.P. Degischer, Met. Mater. Trans. A39 (6) (2008) 1466–1474.
[39] G. Requena, G. Garcés, Z. Asghar, E. Marks, P. Staron, P. Cloetens, Adv. Eng. Mater. 13 (8) (2011) 674–684.
[40] P.Y. Zhu, Q.Y. Liu, T.X. Hou, AFS Trans. 93 (1985) 609–614.
[41] G. Requena, B. Bauer, H.P. Degischer, M. Lieblich, Int. J. Mater. Res. 102 (8) (2011) 982–992.